Supporting Information

One pot solvent assisted syntheses of Ag_3SbS_3 nanocrystals and exploring their phase dependent electrochemical behavior toward oxygen reduction reaction and visible light induced methanol oxidation reaction

Jit Satra,[a] Uday Kumar Ghorui,[a] Papri Mondal,[a] Gopala Ram Bhadu,[b] Bibhutosh Adhikary*[a]

* Corresponding authors

[a] Department of Chemistry, Indian Institute of Engineering Science and Technology, Shibpur, Howrah 711 103, West Bengal, India

Email: bibhutosh@chem.iiests.ac.in

[b] Department of Analytical and Environmental Science Division and Centralized Instrument Facility, Gijubhai Badheka Marg, Bhavnagar 364021, Gujarat, India

Physical Measurement

Powder X-ray diffraction studies have been done using a PAN analytical X-ray diffractometer having monochromatic CuKα radiation (λ = 1.540598 Å). To evaluate the elemental composition, Energy dispersed X-ray (EDX) analysis was performed using a JEOL JSM-7100F. Shape and morphologies were studied using a radiation source JEOL JEM-2100 transmission electron microscope (TEM) working at 200 kV and field emission scanning electron microscopy (FE-SEM JEOL JSM 7100F) operating at 20 kV. X-ray photoelectron spectroscopy (XPS) was performed by Perkin-Elmer Physical Electronics 5600 spectrometer. Absorption spectra of nanoparticle samples were recorded on a JASCO V-530 UV-vis spectrophotometer. Raman spectra were collected on a Micro-Raman spectroscopy system RM 2000 (Renishaw in Via-reflex, 532 nm excitation laser). The surface area of the samples has been obtained by an automatic gas adsorption/desorption analyzer (Quantachrome Instruments, version 3.01) with N_2 as adsorbate. The corresponding samples were degassed in vacuum at 220 °C for 24 h before test. The specific surface areas of the samples were calculated by the Brunauer-Emmett-Teller (BET) method using the adsorption S-3 branch in the relative pressure range from 0.05-0.30. Infrared spectra were obtained in the range of 4000–400 cm^{-1} in liquid phase by JASCO FT-IR-460 Plus.

Device Fabrication for Photoelectrochemical Methanol Oxidation Reaction (PEC-MOR) and Oxygen Reduction Reaction (ORR)

The working electrode for PEC-MOR was fabricated by the drop casting method on indium tin oxide (ITO) coated glass slide. At first, the ITO glass slides were cleaned thoroughly by ultrasonication in water–acetone–iso-propanol respectively for approx. 12 hours. Then a thin

layer of TiO_2 was drop casted by 1µM TiO_2-nafion solution mixture [80 mg of TiO_2 in the mixture of 900 µL H_2O and 100 µL 5 wt% nafion solution] homogenized by long ultrasonication (2 h). The active layer for monoclinic Ag_3SbS_3 (SAS) was drop casted over the ITO coated glass slides by same concentration (538 mg, 1µM) SAS-nafion solution mixture. The photoactive surface area of ITO coated glass slides is maintained at 0.250 cm^2. Then it was dried in air overnight and finally annealed at 50 °C for 1 h under an argon atmosphere. For cyclic voltammetry (CV) of MOR, the same concentration of the corresponding materials is drop casted on the glassy carbon electrode (GCE) having maintained the surface area at 0.126 cm^2 and dried overnight at room temperature.

For ORR, ~5 mg of hexagonal SAS is dispersed in 900 µL H_2O and 0.1 ml 5wt% of nafion solution by ultrasonication to make a homogenized catalyst ink. This catalyst ink was drop casted 10µL at a time by micropipette on to the polished glassy carbon disk of RRDE and the loading of the catalyst was maintained at 0.30 mg/cm^2. The method of Pt loading for commercial Pt/C is similar to the catalyst loading and here the loading was fixed to 0.35 mg/cm^2. The surface area of polished glassy carbon disk electrode is 0.126 cm^2 (electrode instrument RRDE 3A).

The number (*n*) of electron transfer was calculated by Koutecky-Levich(K-L) equation which is as follows:

$$\frac{1}{I} = \frac{1}{I_k} + \frac{1}{I_d} \qquad \textbf{(S1)}$$

I, I_k, and I_d represented as obtained, kinetic and diffusion current densities in $mAcm^{-2}$ respectively. **I_d** can be represented as;

$$I_d = 0.2n\,F\,D^{2/3}\,\nu^{-1/6}\,\omega^{1/2}\,C_{O2} \qquad \textbf{(S2)}$$

n is the number of electron transferred, F is the Faraday constant (96485 c mol^{-1}), D is the diffusion coefficient of O_2 (1.910×10^{-5} cm^2 sec^{-1}) in 0.1(M) KOH, ν is the kinetic viscosity (1.13×10^{-2} cm^2 sec^{-1}), ω represents rotational speeds in rpm, C is the bulk O_2 concentration in 0.1(M) KOH (1.2×10^{-3} mol L^{-1}). The number of electron transferred and percentage of H_2O_2 were calculated by the following equation:

$$n = \frac{4\,I_D}{I_D + I_R/N} \qquad \textbf{(S3)}$$

$$\%H_2O_2 = \frac{200\,I_R}{I_R + I_D\,N} \qquad \textbf{(S4)}$$

Where I_D and I_R are disk and ring current density and N is the collection efficiency which is 0.37. The durability test has been measured in O_2 saturated 0.1(M) KOH with 100 mV/sec scan rate at room temperature.

Electrochemical active surface area (ECSA) for the corresponding samples have been estimated by performing cyclic voltammetry (CV) with different scan rates (20-100 mV/sec) in 1(M) KOH to explore the non-faradic capacitive current associated with double layer charging which leads to obtain double layer charge capacitance (C_{dl}). Linear relation between Δ(current density) (anodic current-cathodic current at 1.2 V Vs. RHE) and scan rate has been fitted and C_{dl} was calculated from the slope of the curve. ECSA and C_{dl} are related by the following equation:

$$\textbf{ECSA} = C_{dl}/C_s \qquad \textbf{(S5)}$$

C_s is solution capacitance for 1(M) KOH (40 μF /cm^2).

Roughness factor (R_F) has also been calculated for corresponding ORR by employing the following equation**:**

$$\mathbf{R_F = (ECSA/active\ area\ of\ electrode)} \qquad \textbf{(S6)}$$

Area of electrode is maintained at 0.125 cm^2.

Electrochemical Characterization of Fabricated Device

CV and Linear Sweep Voltammetry (LSV) experiments were carried out by CHI-700E electcrochemical workstation USA. The whole redox reactions were performed in a three electrode configured cell setup where fabricated RRDE (for ORR) and fabricated ITO coated thin film (for MOR) have been used as working, Ag/AgCl as reference and a Pt wire acted as a counter electrode. The potential used in Ag/AgCl (saturated KCl) has been converted into RHE using equation: $\mathbf{E_{RHE} = E_{Ag/Agcl} + 0.197 + 0.059pH}$**.** The pH of 0.1 (M) KOH is obtained as 12.8. In case of MOR, the electrolyte was taken as mixture of 0.1 (M) KOH and 0.1 (M) MeOH and for ORR the electrolyte was 0.1(M) KOH only. For light source, a photon flux equivalent to 100 mW/cm^2 (1 sun) has been used for PEC MOR. The scan rate was maintained at 100 mV/sec for both MOR and ORR. ORR and MOR are carried out under O_2 and Ar saturated solution respectively.

Nyquist plots by EIS measurement were obtained by Autolab-302N, PG-Stat FRA-II (software NOVA 1.10, Metrohm, Netherlands. For ORR a fixed bias of 0.8 V Vs. RHE is maintained in EIS whereas for MOR the whole experiment was carried out with a fixed bias of 1.0 V Vs. RHE. The frequency range of 1-100000 Hz is maintained for both MOR and ORR. To obtain the flat band potential for the fabricated device, the Mott–Schottky plots were obtained by Impedence-Potential experiment with a fixed frequency of 100000 Hz.

Computational Method Details

All theoretical calculations were studied using CASTEP (Cambridge Sequential Total Energy Package) code which is based on the first principle DFT.[1] The Generalized gradient approximation (GGA) of exchange-correlation potential by Perdew, Burke, and Ernzerhof (PBE) approach was adopted.[2] For Brillouin zone integration the Monkhorst-Pack grid[3] was used and to calculate the electrocnic structure and geometrical relaxation, each k point having wave functions were exaggerated with a plane wave basis set. 2 × 2 × 3 k-point sampling was introduced and a 500eVcut-off was applied for this calculation. The geometry optimization was underdone until the energy was converged to 10^{-6} eV/atom and also we let the forces on the atoms be converged to 0.03 eV/ Å. The value of the total stress was 0.1 GPa and the maximum atomic displacement was between 0.002 Å. The zero point energy (ZPE) was obtained by harmonic vibrational frequency calculations. The overall van der Walls interactions were addressed by DFT-D2 force field approach.

The free energy change between initial state and final state was calculated by following equation (developed by Rossmeisi and Norskov et al)[4] :

$$\mathbf{\Delta G = \Delta E + \Delta ZPE - T\Delta S + \Delta G_U + \Delta G_{pH} + \Delta G_{field}} \qquad \textbf{(S7)}$$

The symbols carry their usual characteristics i.e. ΔE is the total change in energy obtained by DFT, ΔZPE is the change in zero point energy, ΔS is the change in entropy, T is room temperature; 298 K, $\Delta G_U = eU$ where e is the transferred charge and U is the electrode potential, with respect to normal hydrogen electrode (NHE), $\Delta G_{pH} = k_B T \ln 10 \times pH$, where k_B is the Boltzmann constant and pH = 14 (for alkaline reaction medium), ΔG_{field} is the electrical double

layer related free energy correction which can be neglected as in previous studies[5,6] . The free energy for O_2 was obtained to be -4.89 eV at 298 K using equation $O_2 + 2H_2 = 2H_2O$. The overall pressure of the gas phase was maintained at 0.035 bar as a reference. Moreover the free energy corresponding to the OH^- was obtained by the following equation; **$\Delta G(OH^-)=\Delta G(H_2O) - 1/2\Delta G(H_2)$.** ORR mechanistic pathways are as following:

$$O_2 + H_2O + e^- + '*' \rightarrow OOH^* + OH^- \quad \textbf{(S8)}$$

$$OOH^* + e^- \rightarrow O^* + OH^- \quad \textbf{(S9)}$$

$$O_2 + H_2O + e^- \rightarrow OH^* + OH^- \quad \textbf{(S10)}$$

$$OH^* + e^- \rightarrow '*' + OH^- \quad \textbf{(S11)}$$

Where * denotes the active adsorption site.

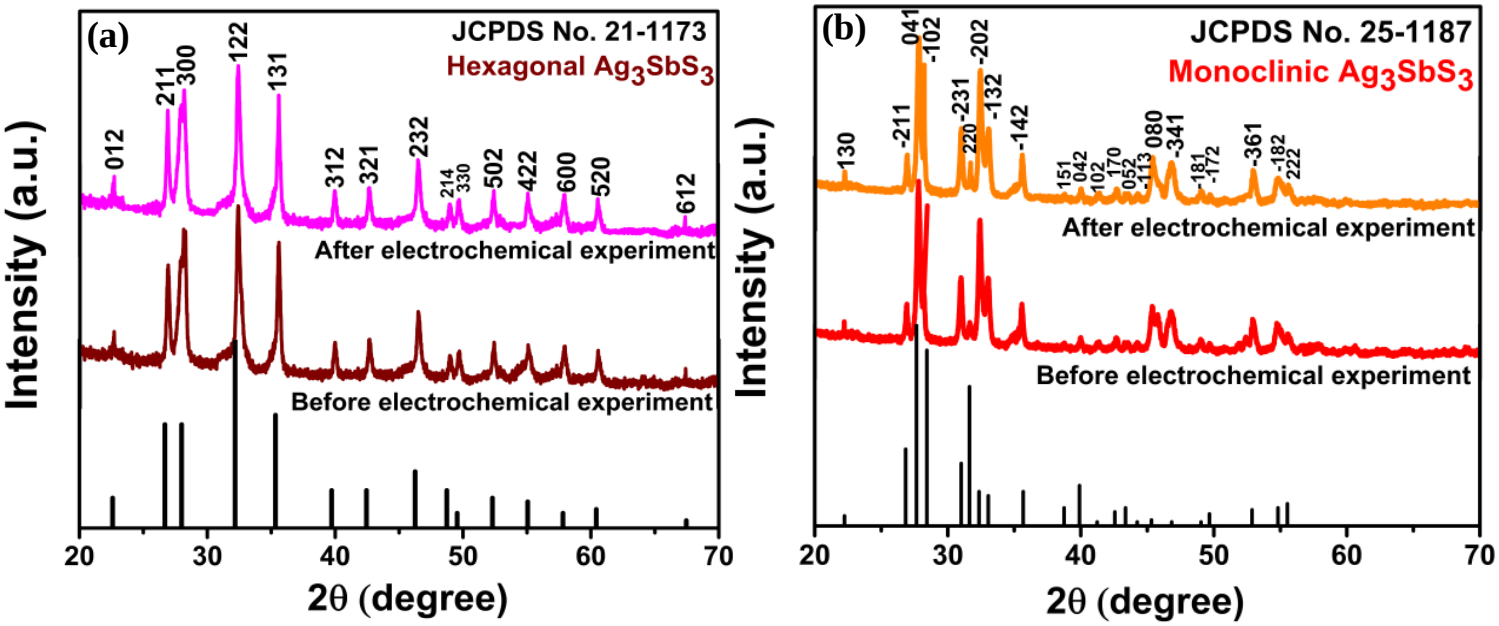

Fig. S1. Powder X-ray diffraction pattern of (a) Hexagonal and (b) Monoclinic; before and after electrochemical experiments.

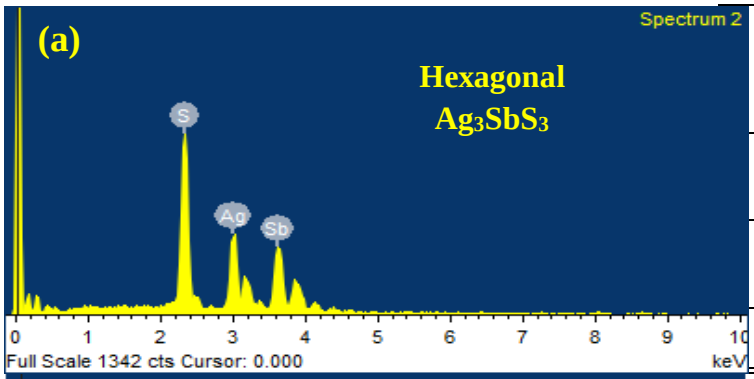

Element	Weight (%)	Atomic (%)
S	21.83	49.98
Ag	37.19	25.31
Sb	40.98	24.71

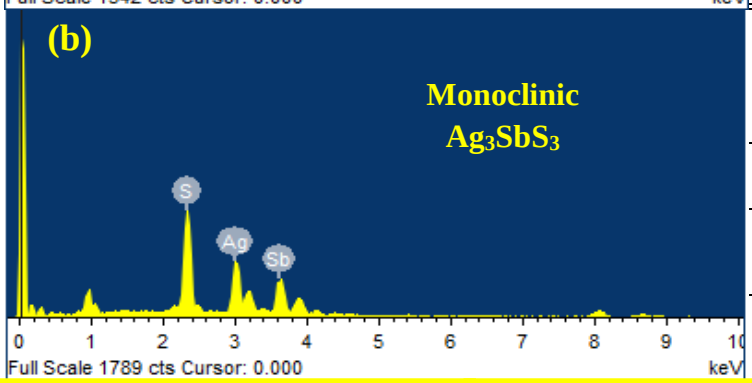

Element	Weight (%)	Atomic (%)
S	22.83	51.58
Ag	32.62	21.91
Sb	44.56	26.52

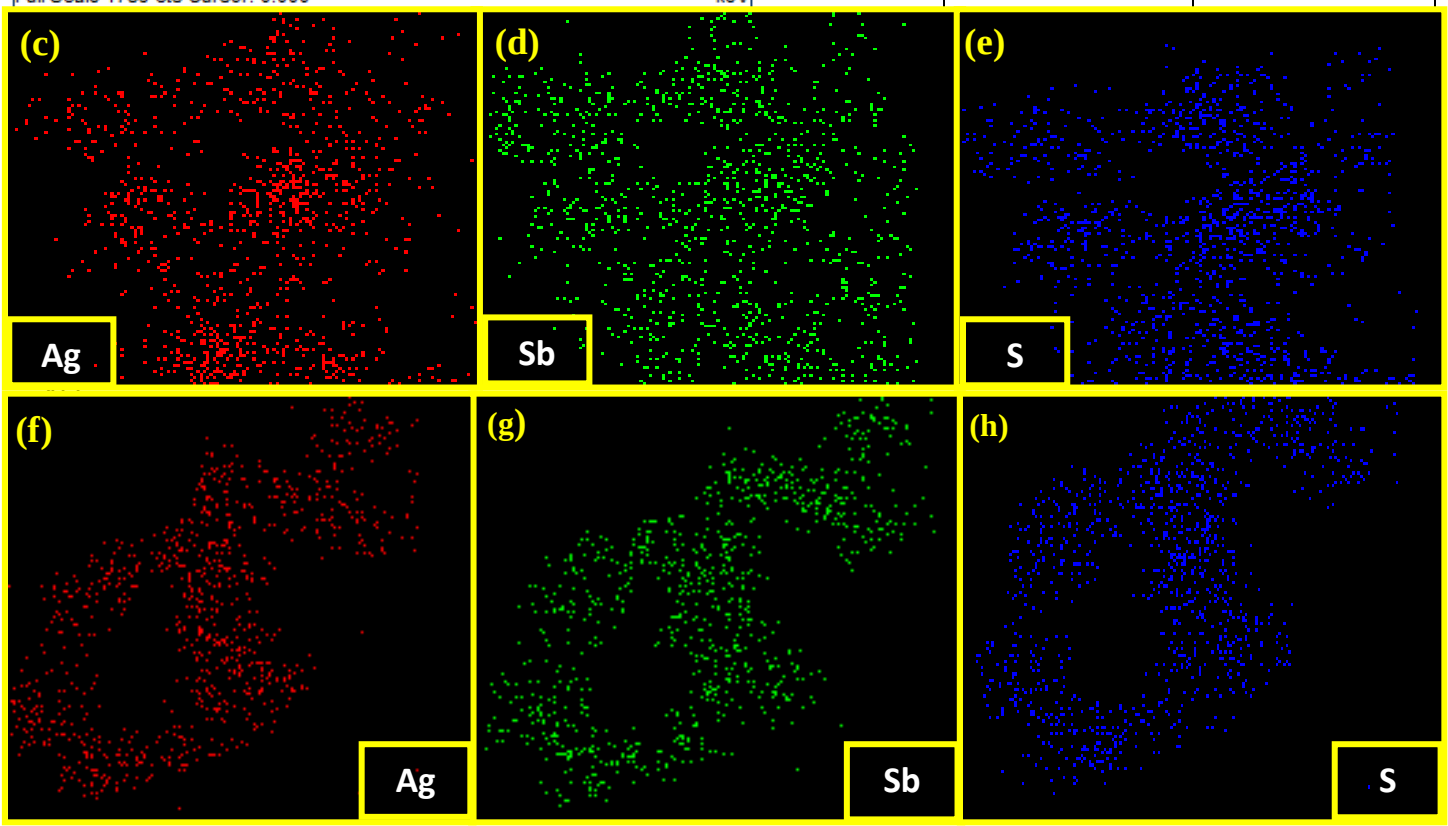

172

Fig. S2. (a) EDX spectra and corresponding elemental composition (right hand side) of monoclinic SAS and (b) EDX spectra and corresponding elemental composition (right hand side) of hexagonal SAS. Elemental mapping for hexagonal SAS are (c) Ag (d) Sb (e) S and for monoclinic (f) Ag (g) Sb (h) S.

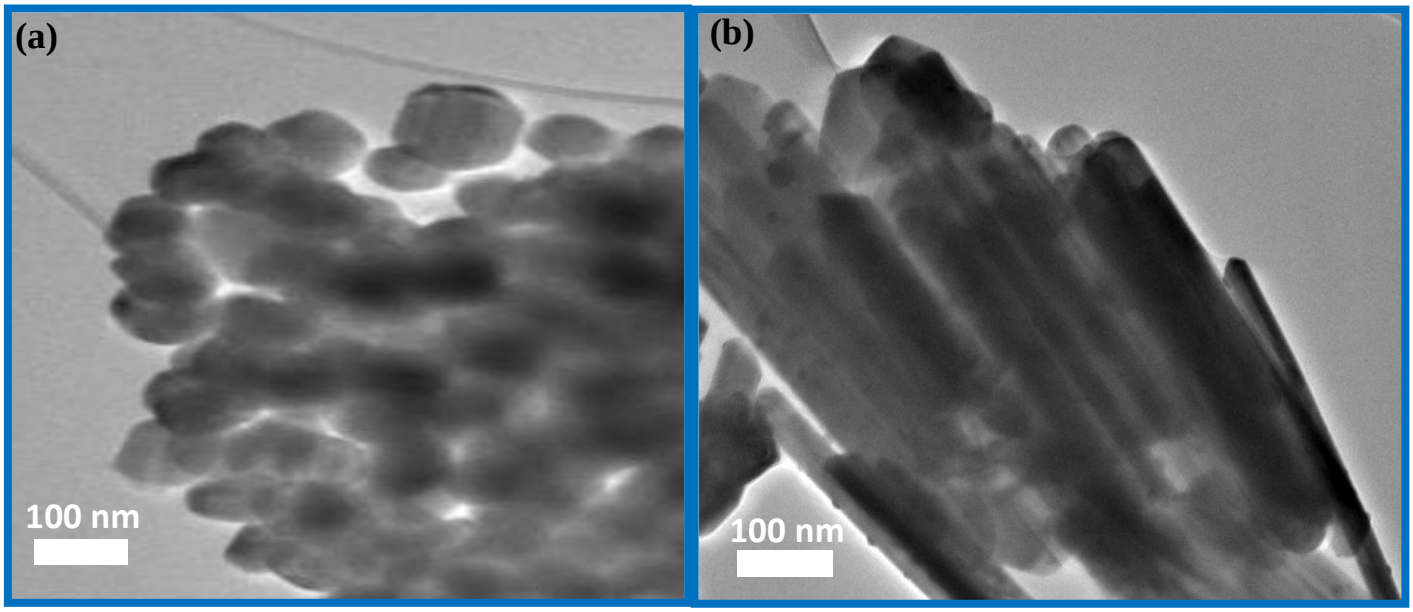

Fig. S3. Morphological analyses by TEM of (a) Hexagonal and (b) Monoclinic SAS after electrochemical experiments.

The tetragonal $[SbS_3]^{-3}$ units of both phases of SAS has C_{3V} symmetry so it is expected to have two stretching modes [ν3(E) and ν1(A1)][7] and the corresponding Raman peaks (Fig. S4) are located at around 303 and 330 cm^{-1} which are red shifted to 310 and 344 cm^{-1} ((a) hexagonal) and to 309 and 382 cm^{-1} ((b) monoclinic). This red shift occurs due to secondary interaction between antimony and sulfur in the crystal system[8]. The extend of this shift for monoclinic system is higher than hexagonal which is attributed to greater extent of secondary interaction as the sulfur atoms might get influenced by Sb more than Ag as already mentioned in the crystal growth section.

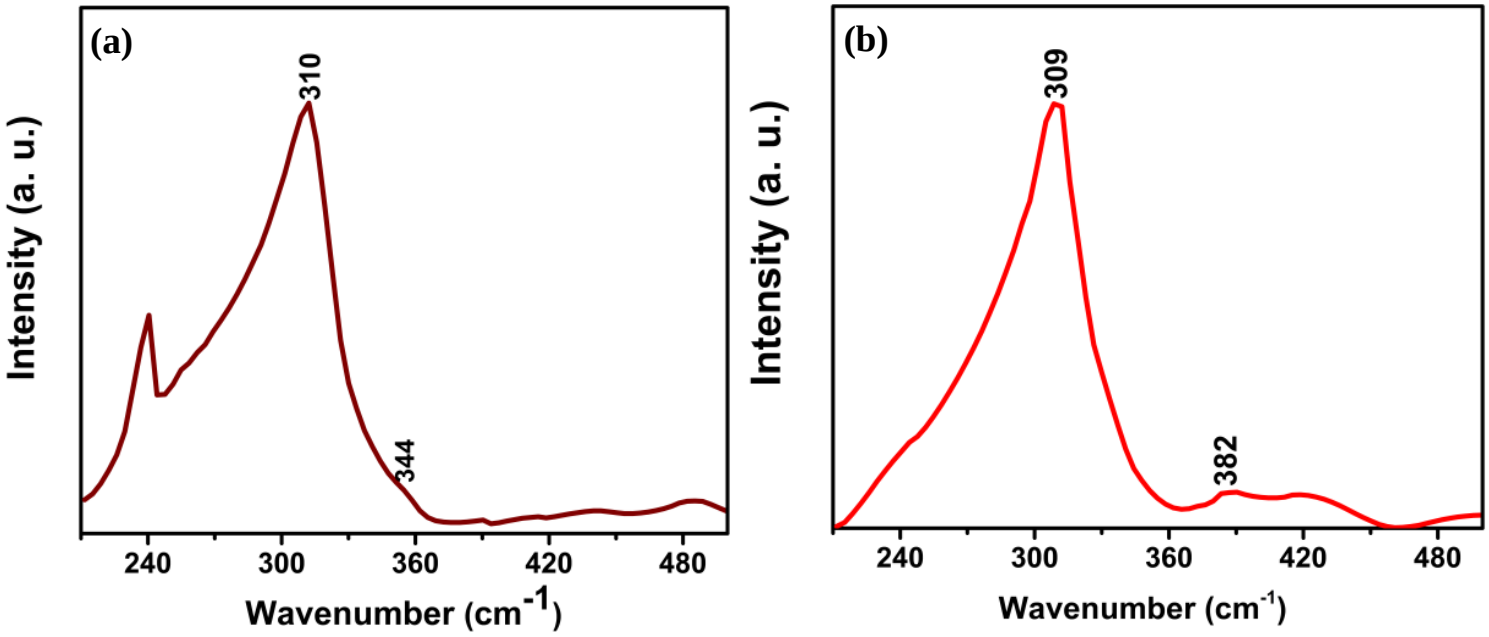

Fig. S4. Raman spectra for (a) hexagonal and (b) monoclinic SAS.

The obtained isotherms are typical IV type BET isotherm, which indicates mesoporous nature of both materials. The very large BET specific surface area was obtained to be 230.10 m^2g^{-1} for hexagonal SAS and 252.85 m^2g^{-1} for monoclinic SAS. The mesoporous nature of the materials has been obtained by the pore size distribution by Barrett–Joyner–Halenda (BJH) experiment shown in insets of corresponding Fig. S5. This exceptionally high surface area for both materials is very beneficial for efficient transport of redox related species like; O_2, OH^- for ORR and CH_3OH, CH_3O^- and OH^- for MOR.[9]

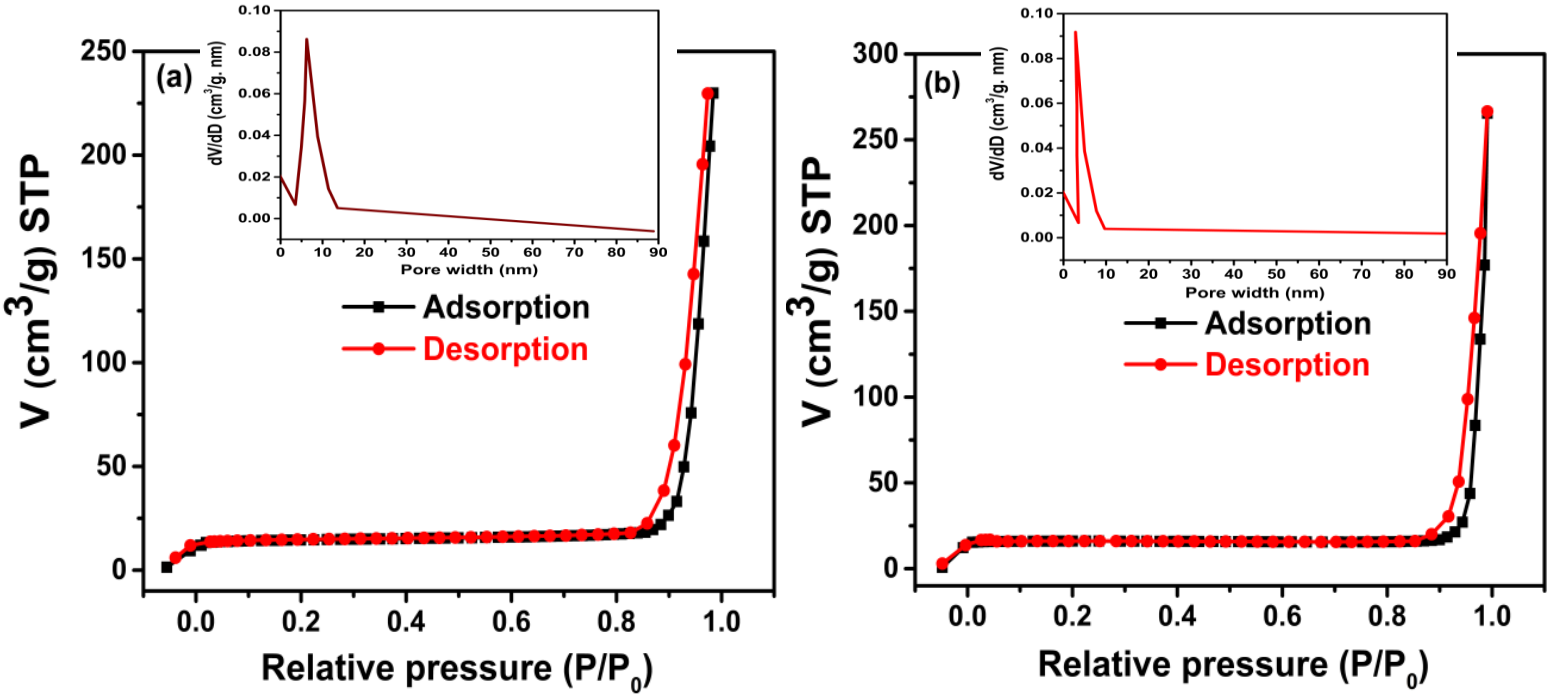

Fig. S5. N_2 adsorption/desorption isotherm plots for (a) hexagonal and (b) monoclinic SAS.

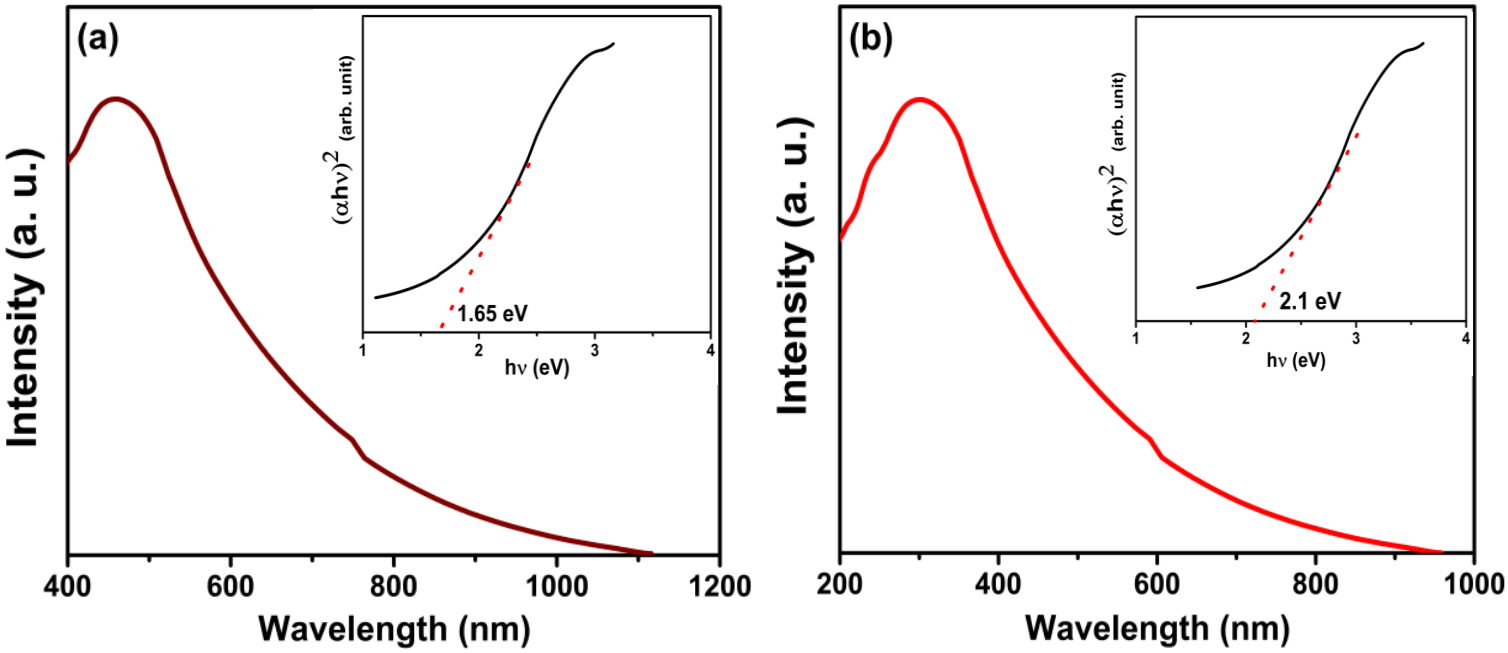

Fig. S6. Electronic spectra for (a) hexagoanl SAS with Tau'c plot (inset) and (b) monoclinic SAS with Tau'c plot (inset)

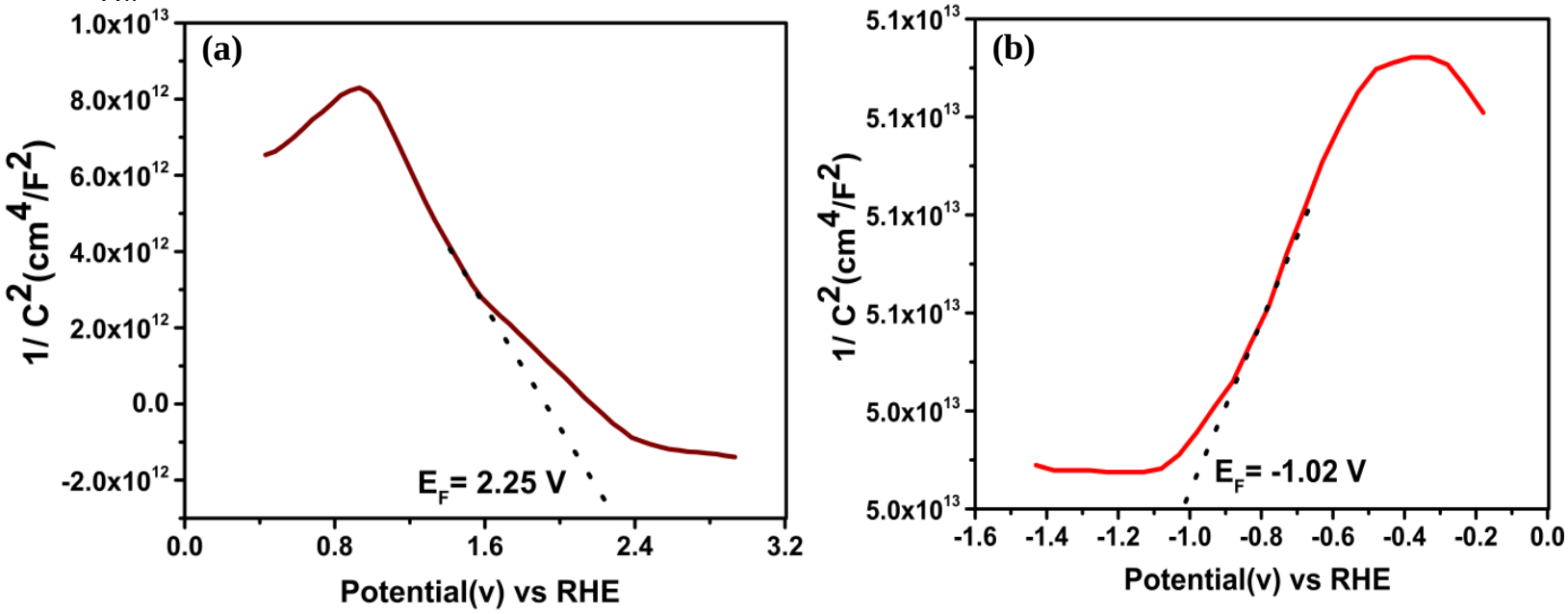

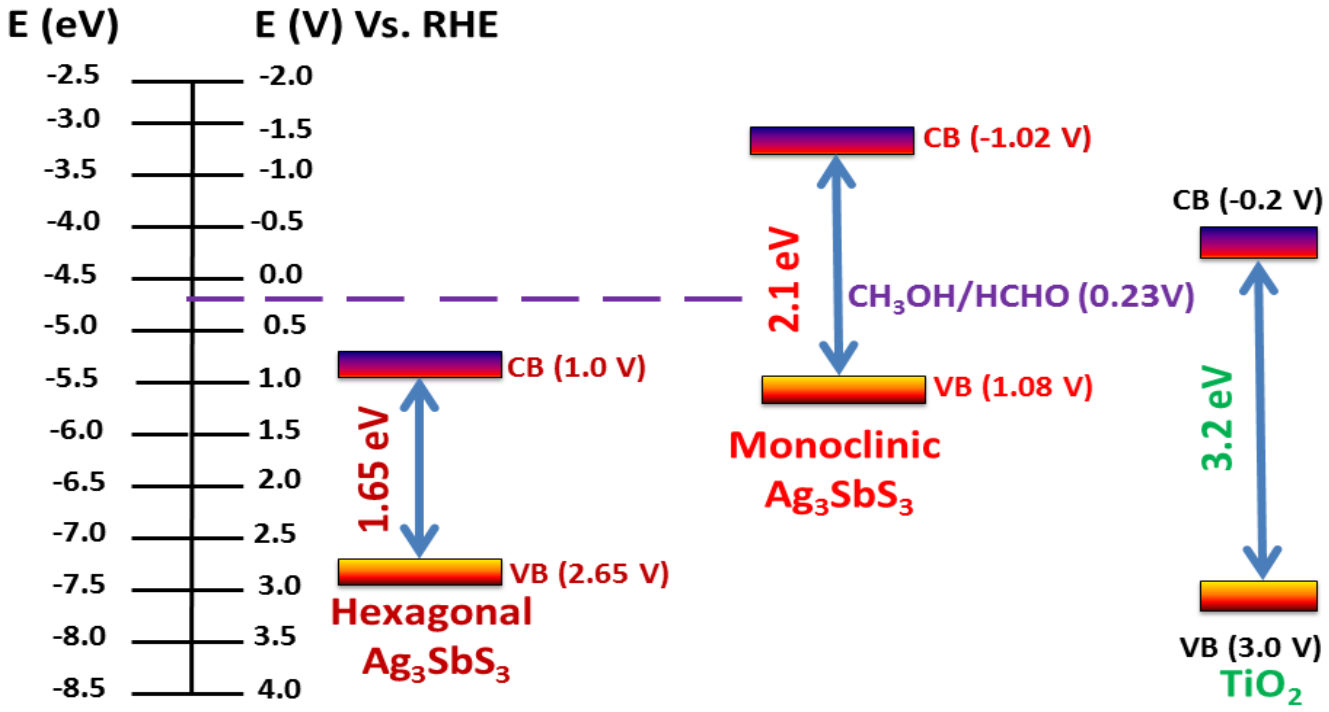

Fig. S7. (a) Mott-schottky plots for (a) hexagonal SAS and (b) monoclinic SAS. (c) Probable energy diagram for ORR and MOR performed by corresponding materials.

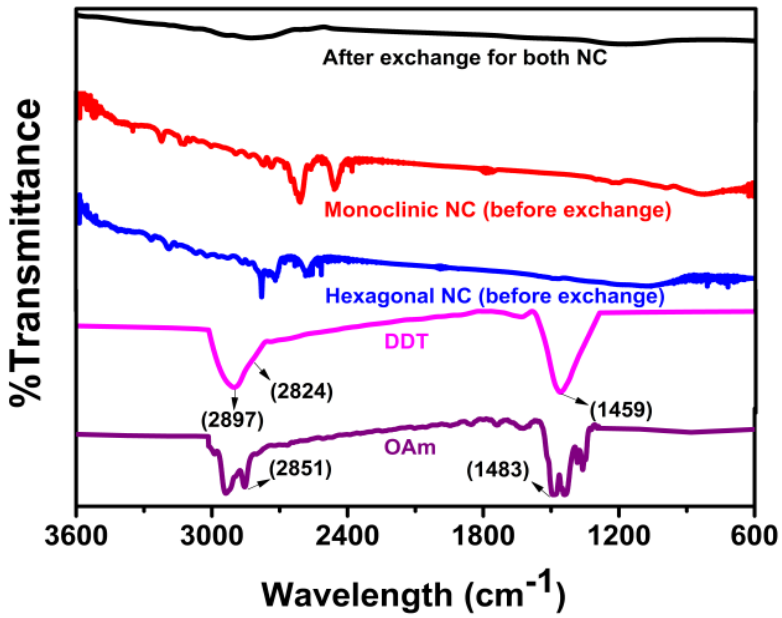

Fig. S8. FTIR spectra for OAm, DDT, Hexagonal NC and Monoclinic NC before and after exchange of organic ligands. Peaks at 2851 and 1483 cm^{-1} for OAm are due to –C-H and -NH_2. Peak at 2824 and 1459 cm^{-1} for DDT are due to =C-H and S-CH_2.[10,11]

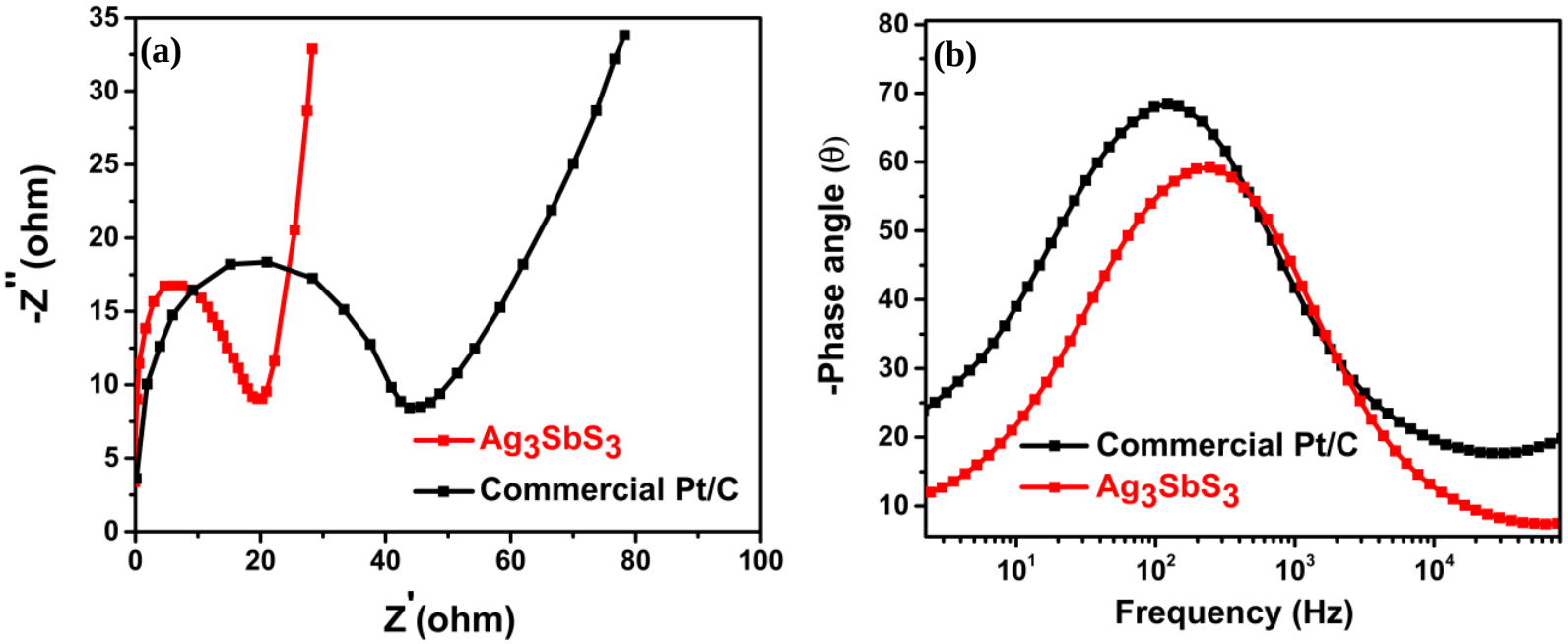

Fig. S9. Comparative EIS study for ORR (a) Nyquist plot (b) Bode plot.

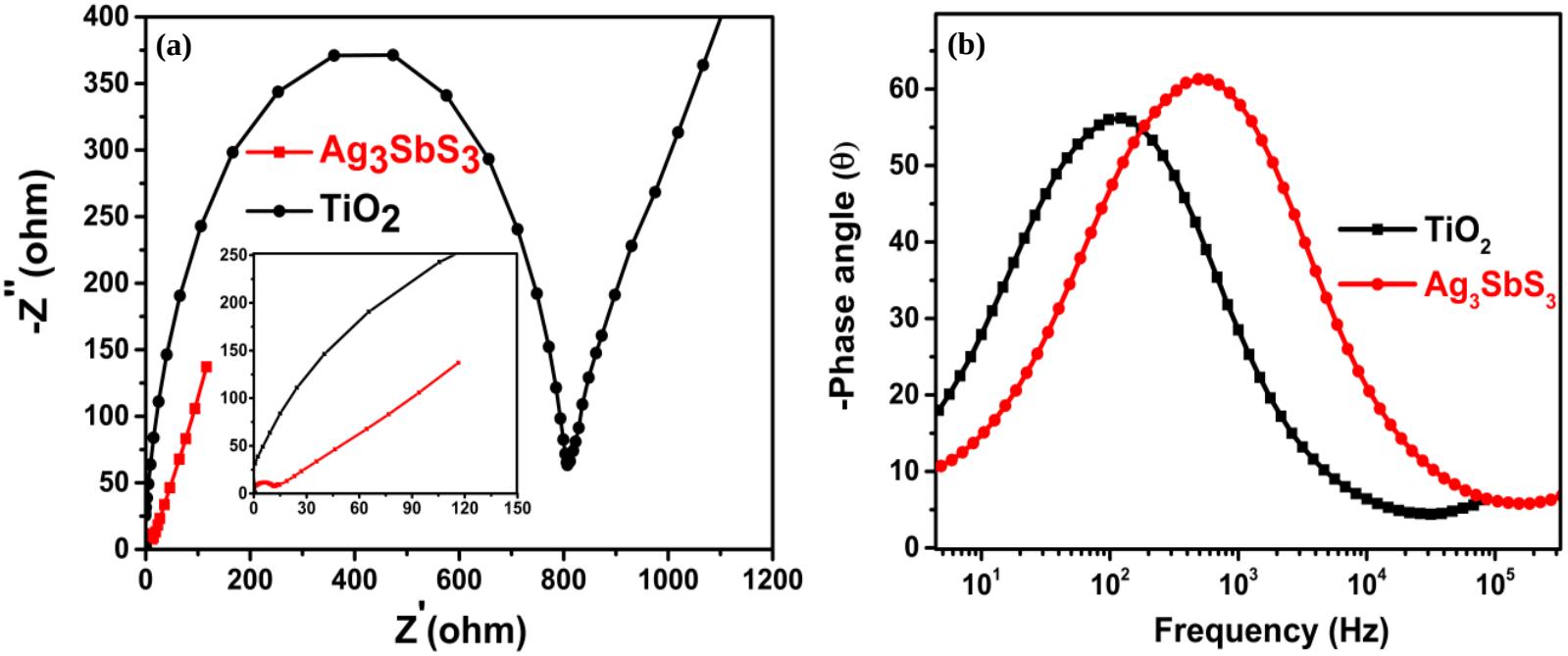

Fig. S10. Comparative EIS study for MOR (a) Nyquist plot (b) Bode plot.

Table S1. Resistance parameters obtained from Nyquist plots.

Materials	R_S **(ohm)**	R_{ct} **(ohm)**
Hexagonal SAS	**3**	**17**
Commercial Pt/C	**4**	**56**
Monoclinic SAS	**6**	**20**
TiO_2	**6**	**741**

In order to have the metal impurities effect for ORR electrochemical reaction on the electrode surface in alkaline electrolytes, we have tested the very low concentration of different transition metals such as Cr, Fe, Co, Ni and Cu by Inductively Coupled Plasma Mass Spectroscopy (ICPMS). We have tabulated the data for different transition metals in various electrolytes. By varying the different grade of chemicals of different batches we have enlisted here only the ranges of concentration (in μg/L) of the following metals in an aqueous solution of the chemicals.

Table S2. The data obtained from ICPMS for the commercial KOH

	Cr	**Fe**	**Co**	**Ni**	**Cu**
Commercial KOH	5-5.2	115.1-115.6	7.2-7.4	11.8-12.1	6.4-6.6

To use the Fe-free KOH electrolytes, we employed a reported method by Boettcher et al[12]. The trace amount of Fe was removed from the KOH electrolyte by highly pure $Ni(OH)_2$ precipitate which acts as an Fe absorbent. The pure precipitate has been obtained by dissolutions of ultrapure $Ni(NO_3)_2.6H_2O$ (99.999%) in ultrapure water in a polypropylene tube. Then 1 (M) KOH was added drop wise to precipitate $Ni(OH)_2$. Then the solution mixture was ultrasonicated

and centrifuged. After centrifugation the supernatant was decanted. This whole procedure was repeated three times. Fig S11 shows ORR polarization curves for different scan in (a) commercial and (b) pure KOH.

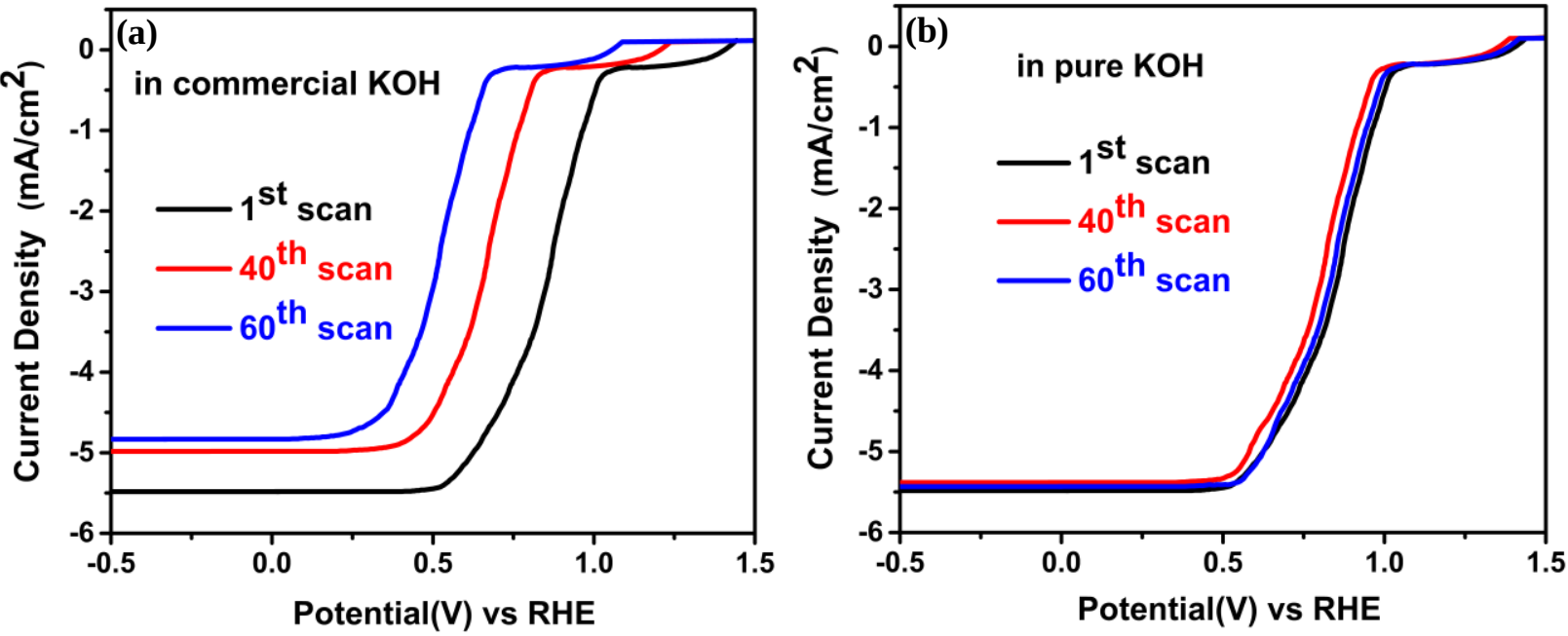

Fig. S11. ORR polarization curve for 1st , 40th and 60th scan (a) in commercial KOH (b) in pure KOH.

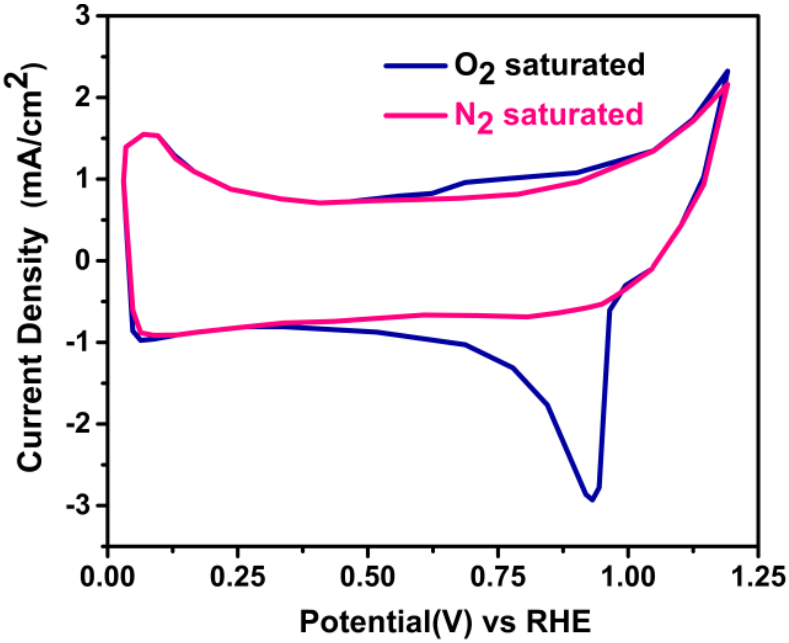

Fig. S12. ORR activity of hexagonal SAS by CV in 0.1 (M) KOH saturated with N_2 and then O_2.

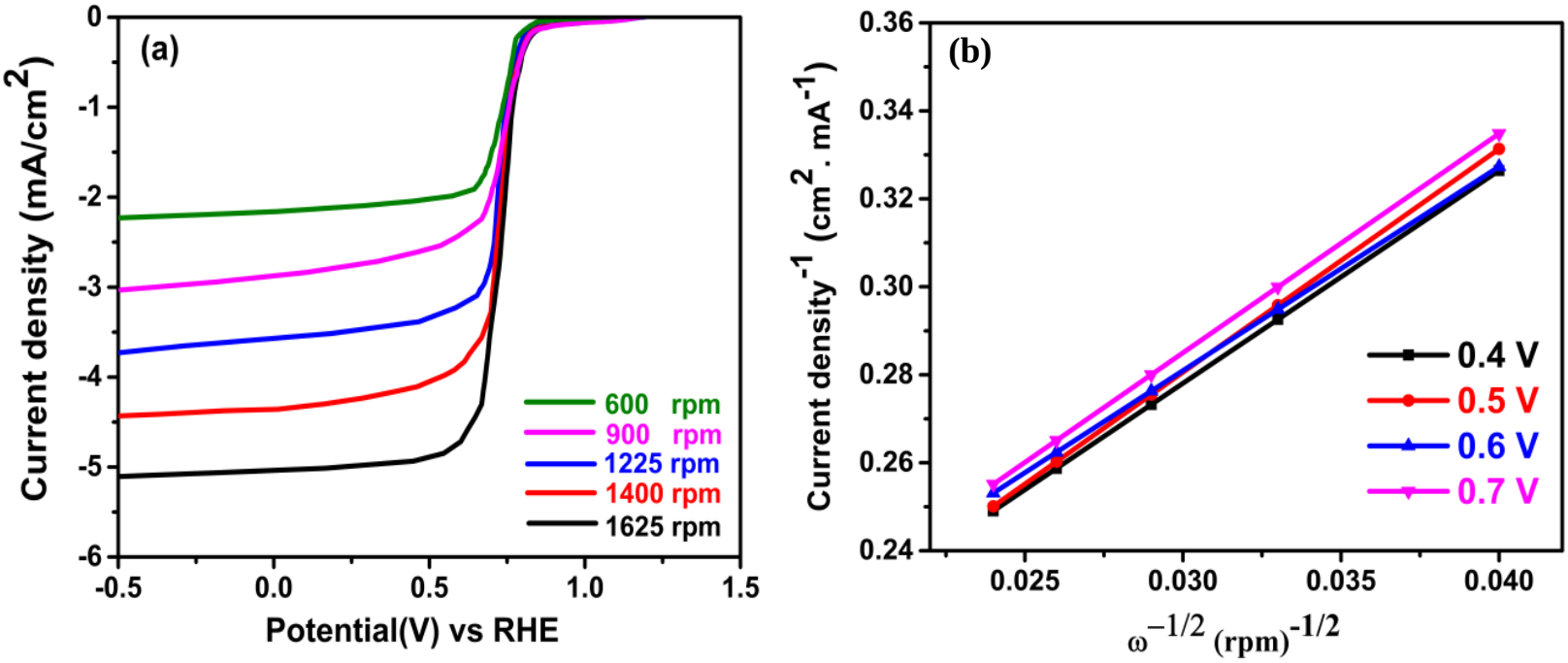

Fig. S13. (a) ORR activity by commercial Pt/C on RRDE with different rotational speed. (b) Corresponding K-L plot to obtain number of electron transferred at different potentials.

Table S3. Specific activity and Mass activity of hexagonal SAS and Pt/C

Material	Specific activity mA.cm^{-2}	Mass activity mA.µg^{-1}
Hexagonal SAS	**1.2**	**0.9**
Commercial Pt/C	**0.7**	**0.5**

.

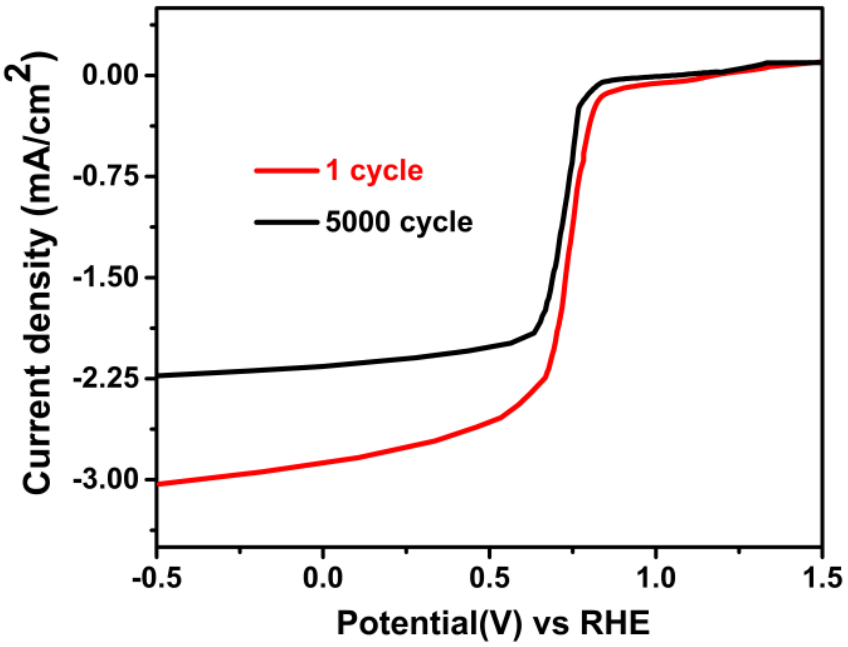

Fig. S14. Durability test by ORR polarization curve for commercial Pt/C from 1st cycle to 5000th cycle

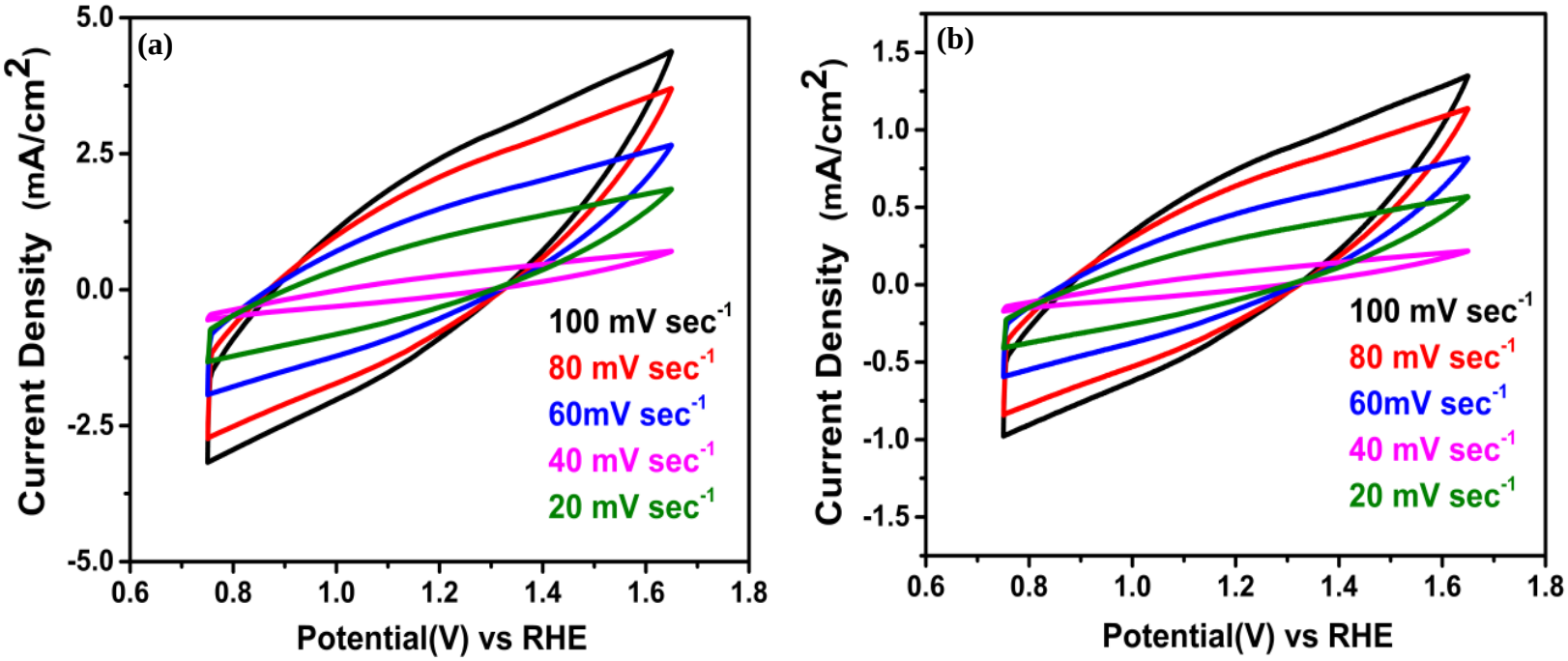

Fig. S15. Cyclic voltammograms (CV) for (a) Hexagonal SAS and for (b) Commercial Pt/C between 0.8-1.6 V Vs. RHE at various scan rates (20, 40, 60, 80 and 100 mV.sec^{-1}).

Table S4. Surface area parameters for corresponding material

Materials	BET ($m^2.g^{-1}$)	C_{dl} ($mF.cm^{-2}$)	ECSA ($m^2.g^{-1}$)	Roughness Factor
Hexagonal SAS	**230.10**	**79.10**	**65.90**	**15,694.44**
Commercial Pt/C	**100.01**[80]	**24.70**	**51.41**	**4,900.79**

The normalized ECSA (Fig. S16) was observed to decrease by 18% in case of hexagonal SAS whereas 48% decrease for commercial Pt/C after 10000 cycles. This result indicates the superior stability of our material leading to higher ORR efficiency than commercial Pt/C.

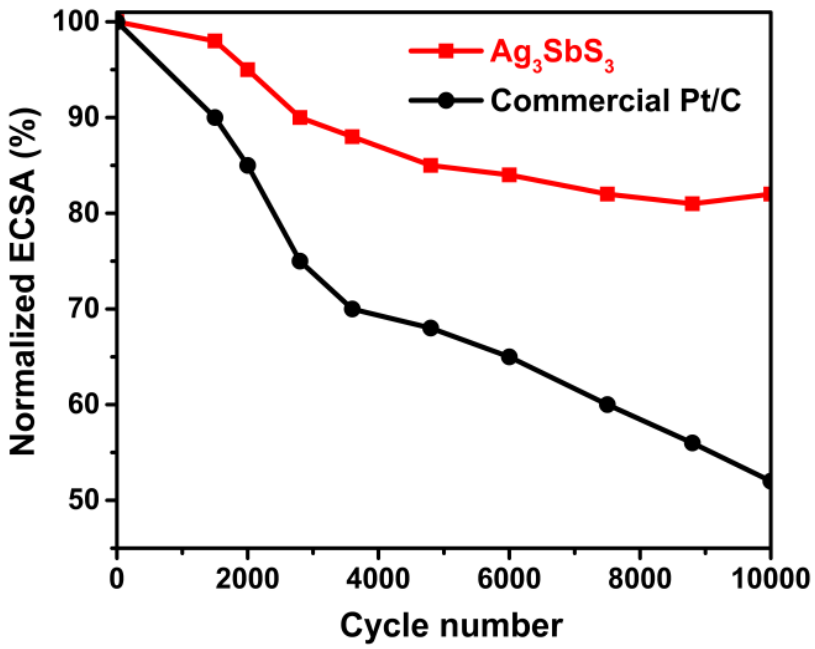

Fig. S16. Loss of normalized ECSA for hexagonal SAS and commercial Pt/C.

The characteristic FTIR spectral (Fig. S17) peaks for aldehyde are appeared at 2922 cm^{-1} [ν_{-CH} (ald)], 1630 cm^{-1} [ν_{-CO} (ald)], 1397 cm^{-1} [ν_{-CH2} (scis) (ald)], 1204 cm^{-1} [ν_{-CH2} (rock) (ald)], 1018 cm^{-1} [ν_{-CH2} (wag) (ald)]. Among these the rate of increase in intensity of the peak at 1630 cm^{-1} is higher than the peak at 2363 cm^{-1} (for formate anion) with time[13] .

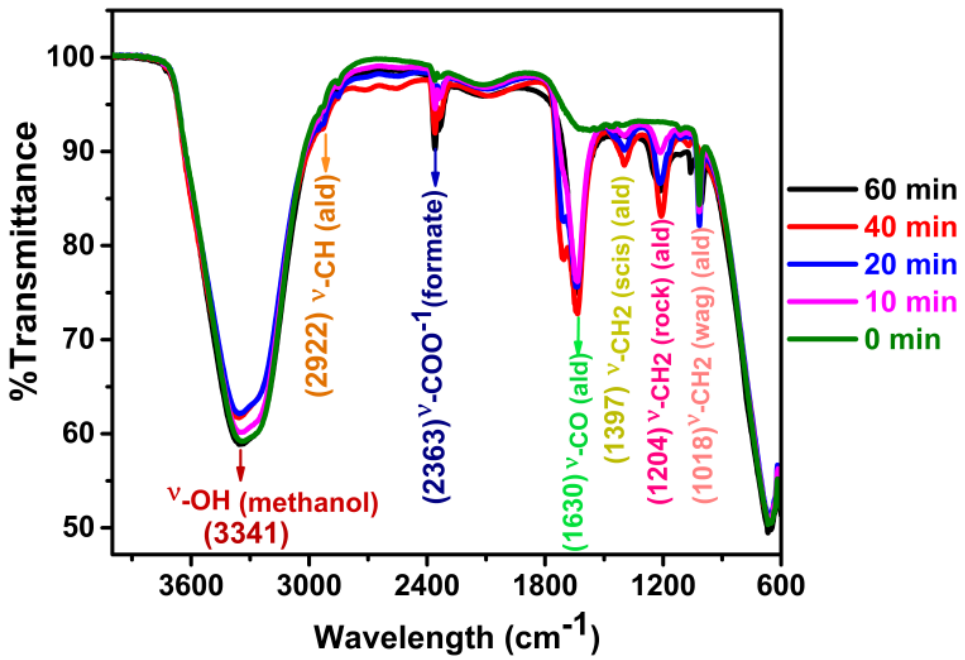

Fig. S17. FTIR spectra for the electrolyte of MOR at different time interval.

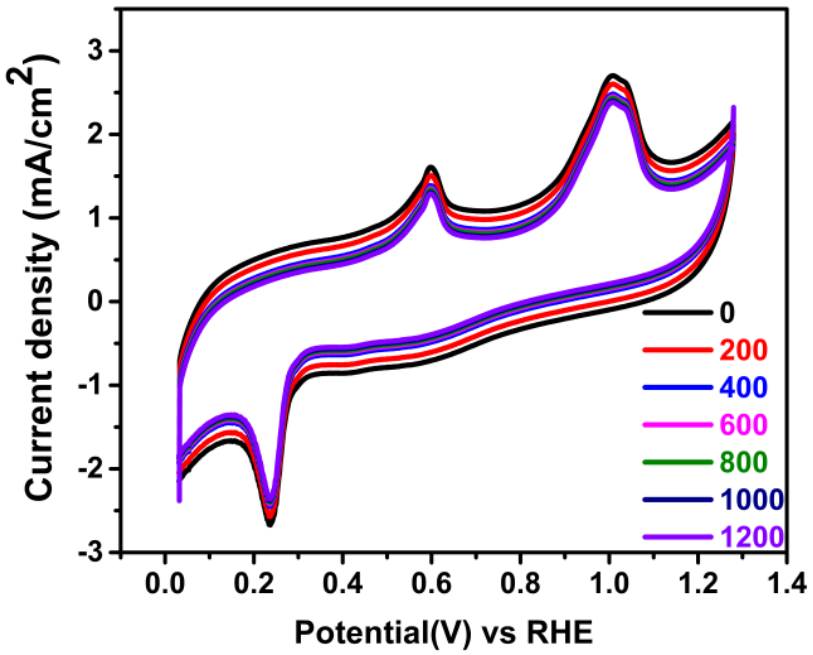

Fig. S18. Stability test by CV for MOR at different electrocatalytic cycles in the mixture of 0.1 (M) KOH and 0.1 (M) MeOH.

Table S5 Comparative data for electrochemical ORR by different ternary metal sulfide semiconductor NCs

Sl. No.	Ternary metal sulfide NCs	Reaction method	Reaction temperature	Reaction time	BET surface area m^2/g	Electrolyte	Catalyst Loading (mg/cm^2)	ORR activity	Year	References
1.	$NiCo_2S4$-SMS	One step solvothermal	220 ^0C	2 h	11.5	0.1 (M) KOH	0.70	E_{Onset} : 0.914 V Vs. RHE, $E_{1/2}$: 0.744 Vs. RHE	2014	14
2.	$NiCo_2S4$-rGO	One step hydrothermal	180 ^0C	12 h	---	0.1 (M) KOH	0.30	E_{Onset} : 0.880 V Vs. RHE, $E_{1/2}$: 0.790 Vs. RHE	2014	15
3.	$NiCo_2S4$/N-CNT	One step hydrothermal	170 ^0C	24 h	73.14	0.1 (M) KOH	1.00	E_{Onset} : 0.930 Vs. RHE, $E_{1/2}$: 0.800 Vs. RHE	2017	16
4.	$NiCo_2S4$@3D GF	One step hydrothermal	160 ^0C	8 h	97.32	0.1 (M) KOH	0.10	E_{Onset} :0.854 V Vs. RHE, $E_{1/2}$: 0.674 Vs. RHE	2017	17
5.	$NiCo_2S4$ HSs	Reflux in solvent mixture	170 ^0C	10 h	23.64	0.1 (M) KOH	0.50	$E_{1/2}$:0.800 Vs. RHE	2018	18

6.	**$NiCo_2S4$@CHNSs**	**Two step hydrothermal**	**180 ^{0}C**	**36 h**	**247.25**	**0.1 (M) KOH**	**0.10**	**E_{Onset} :0.944 V Vs. RHE, $E_{1/2}$:0.764 Vs. RHE**	**2017**	**19**
7.	**S-GNS/$NiCo_2S4$**	**Three step process involving hydrothermal, reflux and sulfurization**	**1st step-160 ^{0}C, 2nd step 80 ^{0}C, 3rd step 300 ^{0}C**	**10 h**	**227**	**0.1 (M) KOH**	**0.42**	**$E_{1/2}$:0.880 Vs. RHE**	**2018**	**20**
8.	**$FeNiS_2$ NSs**	**One step hydrothermal**	**220 ^{0}C**	**1.5 h**	**57.6**	**0.1 (M) KOH**	**0.10**	**E_{Onset} :0.78 V Vs. RHE**	**2016**	**21**
9.	**$CuCoS_4$ NSs**	**One step solvothermal**	**245 ^{0}C**	**10 min**	**---**	**0.1 (M) KOH**	**---**	**E_{Onset} : 0.900 V Vs. RHE, $E_{1/2}$:0.740 Vs. RHE**	**2016**	**22**
10.	**$CoInS_4$/S-rGO**	**One step solvothermal**	**200 ^{0}C**	**18 h**	**102**	**0.1 (M) KOH**	**0.25**	**E_{Onset} :0.93 Vs. RHE, $E_{1/2}$:0.82 Vs. RHE**	**2018**	**23**
11.	**Hexagonal SAS**	**One step solvothermal**	**220 ^{0}C**	**1 h**	**230.10**	**0.1 (M) KOH**	**0.3**	**E_{onset} :1.09 V Vs. RHE and $E_{1/2}$:0.86 V Vs. RHE**	**2020**	**This work**

Table S6 Comparative data for photo induced MOR by various metal based catalyst

Sl No.	Catalyst	Medium	Light used	I_L-I_D/I_D (%)	Year	Reference
1.	PtNi/C-TiO_2 NTs	1.0 (M) NaOH and 0.5 (M) MeOH	Visible	14	2013	24
2.	Pt–WO_3–TiO_2	1.0 (M) KOH and 1 (M) MeOH	Visible	10	2014	25
3.	Pt/TiO_2/BDD	0.5 (M) H_2SO_4 and 1 (M) MeOH	UV	25	2013	26
4.	Pt/SnO_2/GNs	0.5 (M) H_2SO_4 and 1 (M) MeOH	UV	80	2016	27
5.	Pt/ZnO/C	0.5 (M) KOH and 1 (M) MeOH	UV-Visible	123	2017	28
6.	Pt-Ni/TiO_2 NTs	1.0 (M) NaOH and 0.5 (M) MeOH	Visible	31	2011	29
7.	TiO_2-Pt NWs	0.5 (M) H_2SO_4 and 2 (M) MeOH	UV	95	2013	30
8.	Pt/TiO_2 NTs	0.5 (M) H_2SO_4 and 1 (M) MeOH	UV-Visible	47	2017	31
9.	Pt/TiO_2 CNTs	1.0 (M) KOH and 1 (M) MeOH	UV	150	2014	32
10.	Pt-TiO_2 NRs	1.0 (M) KOH and 1 (M) MeOH	UV-Visible	186	2017	33
11.	Monoclinic SAS	0.1 (M) KOH and 0.1(M) MeOH	Visible	845	2020	This work

References

1. S. J. Clark, M. D. Segall, C. J. Pickard, P. J. Hasnip, M. I. J. Probert, K. Refson and M. C. Payne, *Z. Kristallogr*., 2005, **220**, 567–570.

2. J. P. Perdew, K. Burke and M. Ernzerhof, *Phys. Rev. Lett*., 1996, **77**, 3865.

3. H. J. Monkhorst and J. D. Pack, *Phys. Rev. B*., 1976**, *13*,** 5188.

4. C. I. Man, H. Y. Su, F. C. Vallejo, H. A. Hansen, I. J. Martínez, N. G. Inoglu, J. Kitchin, T. F. Jaramillo, J. K. Nørskov and J. Rossmeisl, *ChemCatChem.*, 2011, **3**, 1159.

5. L. Yu, X. Pan, X. Cao, P. Hu and X. Bao, *J. Catal*. 2011, **282**, 183-190.

6. S. Kattel, P. Atanassov and B. Kiefer, *J. Phys. Chem. C.*, 2012, **116**, 17378-17383.

7. A. Pfitzner, *Inorg. Chem*., 1998, **37,** 5164-5167.

8. A. Pfitzner, *Chem. Eur. J*., 1997, **3,** 2032-2038**.**

9. R. Zhang, C. Zhang and W. Chen, *J. Mater. Chem. A.*, 2016, **4 (48),** 18723–18729.

10. B-Q. Zhang, Y. Liu, Y. Zuo, J-S. Chen, J-M. Song, H-L. Niu, C-J. Mao, *Nanomaterials.*, 2018, 8, 8-12.

11. Y. Xu, L. Yuan, R. Xie, L. Wang, Q. Liang, Z. Geng, H. Liu and K. Huang, *Cryst. Growth Des*., 2018, **18**, 864–871.

12. L. Trotochaud, S. L. Young, J. K. Ranney and S. W. Boettcher, *J. Am. Chem. Soc*., 2014, **136,** 6744-6753.

13. M. I. Alkhalf and M. E. S. Mirghani, *International Food Research*., 2017, **24**, S496-S500.

14. Z. Zhang, X. Wang, G. Cui, A. Zhang, X. Zhou, H. Xu and L. Gu, *Nanoscale.*, 2014, **6**, 3540–3544. .

15. J. Wu, S. Dou, A. Shen, X. Wang, Z. Ma, C. Ouyang and S. Wang, *J. Mater. Chem. A.*, 2014, **2**, 20990–20995.

16. X. Han, X. Wu, C. Zhong, Y. Deng, N. Zhao and W. Hu, *Nano Energy*, 2017, **31**, 541–550.

17. X. Wu, S. Li, B. Wang, J. Liu and M. Yu, *New J. Chem.*, 2017, 41, 115–125.

18. X. Feng, Q. Jiao, H. Cui, M. Yin, Q. Li, Y. Zhao, H. Li, W. Zhou and C. Feng, *ACS Appl. Mater. Interfaces*, 2018, **10**, 29521–29531.

19. X. Wu, S. Li, B. Wang, J. Liu and M. Yu, Phys. *Chem. Chem. Phys.*, 2017, **19**, 11554-11562.

20. W. Liu, J. Zhang, Z. Bai, G. Jiang, M. Li, K. Feng, L. Yang, Y. Ding, T. Yu, Z. Chen and *A. Yu*, *Adv. Funct. Mater*, 2018, **28**, 1706675.

21. J. Jiang, S. Lu, H. Gao, X. Zhang and H.-Q. Yu, *Nano Energy*, 2016, **27**, 526–534.

22. S. Zhao, Y. Wang, Q. Zhang, Y. Li, L. Gu, Z. Dai, S. Liu, Y.-Q. Lan, M. Han and J. Bao, *Inorg. Chem. Front.*, 2016, **3**, 1501–1509**.**

23. G. Fu, J. Wang, Y. Chen, Y. Liu, Y. Tang, J. B. Goodenough and J.-M. Lee, *Adv. Energy Mater.*, 2018, **8**, 1802263**.**

24. H. He, P. Xiao, M. Zhou, F. Liu, S. Yu, L. Qiao and Y. Zhang, *Electrochim. Acta*, 2013, **88**, 782–789.

25. C. Wang, F. Jiang, R. Zhou, Y. Du, P. Yang, C. Wang and J. Xu, *Mater. Res. Bull.*, 2013, **48**, 1099–1104.

26. T. Spătaru, M. Marcu and N. Spătaru, *Appl. Surf. Sci.*, 2013, **269**, 171–174.

27. F. Lei, Z. Li, L. Ye, Y. Wang and S. Lin, *Int. J. Hydrogen Energy*, 2016, **41**, 255–264.

28. X. Hu, C. Ge, N. Su, H. Huang, Y. Xu, J. Zhang, J. Shi, X. Shen and N. Saito, *J. Alloys Compd.*, 2017, **692**, 848–854.

29. H. He, P. Xiao, M. Zhou, Y. Zhang, Y. Jia and S. Yu, *Catal. Commun.*, 2011, **16**, 140–143.

30. J. K. Oh, Y. W. Lee and K. W. Park, *J. Ind. Eng. Chem.*, 2013, **19**, 1391–1394.

31. J. Zhang, N. Su, X. Hu, F. Zhu, Y. Yu and H. Yang, *RSC Adv.*, 2017, **7**, 56194–56203.

32. J. Huang, J. Zang, Y. Zhao, L. Dong and Y. Wang, *Mater. Lett.*, 2014, **137**, 335–338.

33. S. Hu, B. Wang, H. Ju, L. Jiang, Y. Ma and Y. Fan, *J. Taiwan Inst. Chem. Eng.*, 2017, **80**, 533–539.